

Research Article

<https://doi.org/10.1631/jzus.A2600179>

A tunable gated strain sensor integrating detachable metamaterial structures for personalized motion recognition

Ziao SHEN^{1,2,3}, Minjian WANG^{1,2,3}, Xiujun FU^{1,2,3}, Guangqiang ZHANG^{1,2,3}, Xiangtao PAN^{1,2,3}, Ye QIU^{1,2,3}, Yi SONG^{1,2,3}, Aiping LIU⁴, Ye TIAN^{1,2,3}✉, Huaping WU^{1,2,3}✉

¹College of Mechanical Engineering, Zhejiang University of Technology, Hangzhou 310023, China

²Zhejiang Key Laboratory of High-Precision and Efficiency Hybrid Processing Technology and Equipment, Zhejiang University of Technology, Hangzhou 310023, China

³Key Laboratory of Special Purpose Equipment and Advanced Processing Technology, Ministry of Education, Zhejiang University of Technology, Hangzhou 310023, China

⁴Center for Optoelectronics Materials and Devices, Zhejiang Sci-Tech University, Hangzhou 310018, China

Abstract: Developing gated strain sensors with high sensitivity and a wide sensing range is crucial for medical supervision, motion monitoring, and human-machine interaction tasks. However, traditional gated sensors lack real-time tunability after fabrication and have a limited tunable range. Herein, we propose a design that integrates a detachable negative Poisson's ratio metamaterial structure with a gated flexible strain sensor. By using a detachable metamaterial layer with a tailored Poisson's ratio, the local strain field distribution during stretching can be effectively modulated, enabling controllable regulation of the gated structure's closure behavior. Through systematic adjustment of the embedment depth, thickness, and microstructural dimensions of the perforated plate metamaterial, bidirectional tunability of the sensing response regime is realized, enabling full-range coverage from 0% to 100% strain. Additionally, the sensor exhibits high sensitivity (a gauge factor of 3049), an ultralow limit of detection (0.05%), a fast response time (100 ms), exceptional stability (negligible variation over 2000 cycles), and excellent frequency adaptability. A smart resistance band system is developed to demonstrate personalized movement recognition for users of varying heights performing exercises such as dips and curls. This work establishes a new paradigm for tunable strain sensors, with promising implications for smart personalized athletic and health monitoring devices.

Key words: Strain sensor; Gated structure; Negative Poisson's ratio; High sensitivity; Wide sensing range; Small strain detection; Personal health monitoring; Wearable smart sports sensors

1 Introduction

With the rapid advancement of flexible electronics, flexible strain sensors – being pivotal tools for real-time monitoring of mechanical deformations – have demonstrated broad application prospects in fields such as biomedical engineering, wearable devices, soft robotics, and human-machine interfaces (Dai et al., 2024; Yang et al., 2025; Luo et al., 2026; Lu et al., 2026; Ma et al., 2025; Yang et al.,

2024; Kong et al., 2025; Song et al., 2026; Liu et al., 2018; Wang et al., 2026; Qiu et al., 2024; Zhang et al., 2024; Luo et al., 2025; Shi et al., 2020). These sensors can conform to complex curved surfaces to achieve continuous, non-invasive monitoring of physiological signals (such as vascular pulsation and muscle movement) or environmental stimuli (such as pressure and deformation); this helps overcome the inherent limitations of conventional rigid sensors with regards to stretchability and biocompatibility (Lou et al., 2019; Wang et al., 2019; Shi et al., 2024). An ideal flexible sensor should possess high sensitivity, high stability, a wide strain range, rapid response time, and soft mechanical properties that are compatible with biological tissues. Among various sensing mechanisms, resistive strain sensors have become a popular research topic due to their simple working

✉ Huaping WU, wuhuaping@gmail.com

Ye TIAN, tianye@zjut.edu.cn

✉ Ye TIAN, <https://orcid.org/0000-0002-4068-7201>

principle, convenient signal readout, and ease of fabrication (Gould, 2018; Bayoumy et al., 2021; Ruan et al., 2024; Qiu et al., 2020). To enhance sensitivity, researchers have proposed diverse design strategies such as geometric structural design (Zhu and Cheng, 2018; Yang, 2020; Lan et al., 2026), crack propagation effects (Kang et al., 2014; Wang et al., 2014; Yin et al., 2017; Yang et al., 2024), and tunneling effects (Xing et al., 2019; Zhong et al., 2024; Qaiser et al., 2021; Zhou et al., 2020; Xue et al., 2019; Wang et al., 2018). Notably, emerging gated sensors often introduce micropillars into liquid channels to control the conduction paths, causing a sharp reduction in the cross-sectional area of the conductive pathway upon stretching, and consequently leading to a drastic change in resistance (Yao et al., 2024; Chi et al., 2014). Although sensing performance can be tuned by designing the spacing of the gated micropillars, in practice this approach requires switching between different sensors (Luo et al., 2023; Yao et al., 2024; Yao et al., 2026), which not only precludes real-time tunability within a single device but also significantly increases fabrication costs and system complexity. Therefore, it is desirable to achieve tunable performance within a single sensor without compromising its sensing capabilities.

Mechanical metamaterials offer a novel pathway to modulate the effective mechanical parameters of materials, such as Poisson's ratio. Poisson's ratio is a dimensionless quantity measuring the ratio of transverse to axial dimensional changes when an elastic material is subjected to axial compression or stretching; it serves as a fundamental mechanical property of materials (Wang et al., 2023). Under external forces, structures with negative Poisson's ratios exhibit deformation behaviors that differ distinctly from those of conventional materials, in particular expanding transversely during axial stretching or contracting transversely during axial compression (Jiang et al., 2018; Yao et al., 2021; Mao et al., 2022; Yan et al., 2023; Kang et al., 2025; Lee et al., 2024; Wang et al., 2026). Shape memory polymer-based composites provide effective support for the fabrication and functional regulation of negative Poisson's ratio structures, enabling flexible modulation of structural morphology and mechanical properties through multi-stimulus responses (Shi et al., 2024; Shi et al., 2024; Lu, 2024; Yao et al., 2018;

Yao et al., 2018; Yao et al., 2018). The regional grouping optimization strategy for complex structures also offers a reference for the functional design of sensors (Zeng et al., 2026; Peng et al., 2026). Since the gated mechanism relies on the positive Poisson's effect, we hypothesize that altering the overall Poisson's ratio of the device can regulate its gating behavior. This concept motivates the use of negative Poisson's ratio metamaterials to develop tunable flexible strain sensors, establishing a theoretical foundation for gated flexible strain sensors with tunable sensing performance.

In this study, a novel design strategy integrating a detachable negative Poisson's ratio metamaterial structure with a gated flexible strain sensor is proposed. By designing a metamaterial attachment layer with a specific Poisson's ratio, the local strain distribution of the sensor can be actively modulated under mechanical loading, optimizing the closure behavior of the gated structure. This strategy not only ensures performance stability but also enables real-time regulation of the sensor's working range. Furthermore, a wedge-shaped gated micropillar structure is established to enhance the sensitivity of the sensor. As a proof-of-concept design, gated sensors integrated with detachable metamaterial structures are assembled into a smart resistance band system, demonstrating their potential for personalized applications such as sports injury prevention and human motion monitoring.

2 Experimental method

2.1 Fabrication of the perforated plate-based negative Poisson's ratio metamaterial layer

The perforated plate structure was fabricated using a Form 2 stereolithography (SLA) 3D printer with Flexible 80A resin (Formlabs Inc.). The printed plates were rinsed in alcohol for 30 seconds and then cleaned in an ultrasonic bath for 5 minutes. A flexible substrate layer was first prepared using Ecoflex 00-30 (Smooth-on Inc.). Then the printed perforated plate structure was placed onto this substrate, followed by the addition of more Ecoflex and thermal curing to obtain a tuning layer embedded with a perforated plate structure.

2.2 Fabrication of the wedge-shaped micropillar

gated strain sensor

The Ecoflex 00-30 (Smooth-on Inc.) mixture was poured onto a microchannel mold and a glass Petri dish, followed by spin-coating and thermal curing at 80 °C for 1 hour. The resulting encapsulation layer and microchannel layer were then treated with surface plasma, bonded together under pressure for approximately 3 minutes, and perforated with small holes at both ends of the microchannel. An ionic liquid ([Emim]BF₄, Shanghai Macklin Biochemical Co., Ltd.) was drop-cast into the holes and automatically filled the microchannel via capillary action. Copper wires were subsequently inserted into the holes to serve as electrodes, and the connection areas were sealed with additional Ecoflex to complete the integrated strain sensor.

Performance characterization was conducted using a universal tensile testing machine (Instron LEGEND-2345), a biaxial stretching stage (PDV PT-SD35), and a semiconductor parameter analyzer (Keithley 4200-SCS). For motion monitoring applications, signals were collected with an LCR meter (HIOKI IM3536). Various tensile tests were performed on the strain sensor using the universal tensile testing machine and the biaxial stretching stage, while the sensor was connected to the semiconductor parameter analyzer for real-time monitoring of resistance variations during stretching.

2.3 Finite element simulation of gated structures and perforated plates

Finite element analysis was conducted using the commercial software Abaqus 2023. The flexible substrate measured 20 mm in length, 20 mm in width, and 1 mm in thickness; the square micropillar was modeled as a cube with a side length of 1.5 mm. The wedge-shaped micropillar was derived from the square micropillar by connecting the midpoints of three sides on its upper surface, forming a pentagonal micropillar. The spacing between adjacent micropillars was set to 0.5 mm. This entire assembly was modeled as an incompressible Mooney–Rivlin material, with material constants of $C_{10} = 0.144$, $C_{01} = 0.036$, and $D_1 = 0.1$. The perforated plate unit cell

had a density of 970 kg/m³, a Young's modulus of 750 kPa, and a Poisson's ratio of 0.49. The boundary conditions are illustrated in Fig. S9 (Supporting Information).

3 Results and discussion

3.1 Mechanism of the perforated plate-based gated strain sensor

Resistive strain sensors translate mechanical deformation into variations in electrical resistance. As has been extensively demonstrated, enhancing the sensitivity requires maximizing the strain responsiveness of the conductive pathways [37,38]. Inspired by biological mechanically-gated ion channels, discretely distributed micropillars are employed as mechanical "gates" to control conduction. The conductive pathway of the interstitial ionic liquid is directly regulated by the non-uniform strain at the pillar–substrate interface. Upon substrate stretching, a transverse contraction is induced at the micropillar–substrate junction by the Poisson effect, whereas the upper portions of the micropillars remain largely undeformed. The inter-pillar gaps are narrowed or completely sealed by this non-uniform deformation, mimicking the closure of a physical gate. In the "open" state, a broad conductive pathway is provided by the ionic liquid-filled gaps. Conversely, when the channel is stretched and the gates are narrowed and closed, the conductive pathway is abruptly constricted, leading to an increase in resistance that is several orders of magnitude. Building upon this mechanism, we design a wedge-shaped micropillar structure (Fig. 1a). Similar to conventional square micropillars, the closure of microchannels under axial stretching is enabled by this architecture. However, because of its unique geometric features, a more pronounced abrupt change in contact area and severe stress concentration are exhibited by the wedge-shaped structure under strain. These effects manifest as an intense and abrupt surge in resistance, resulting in a more substantial overall resistance change for the sensor under identical strain conditions (Fig. 1c).

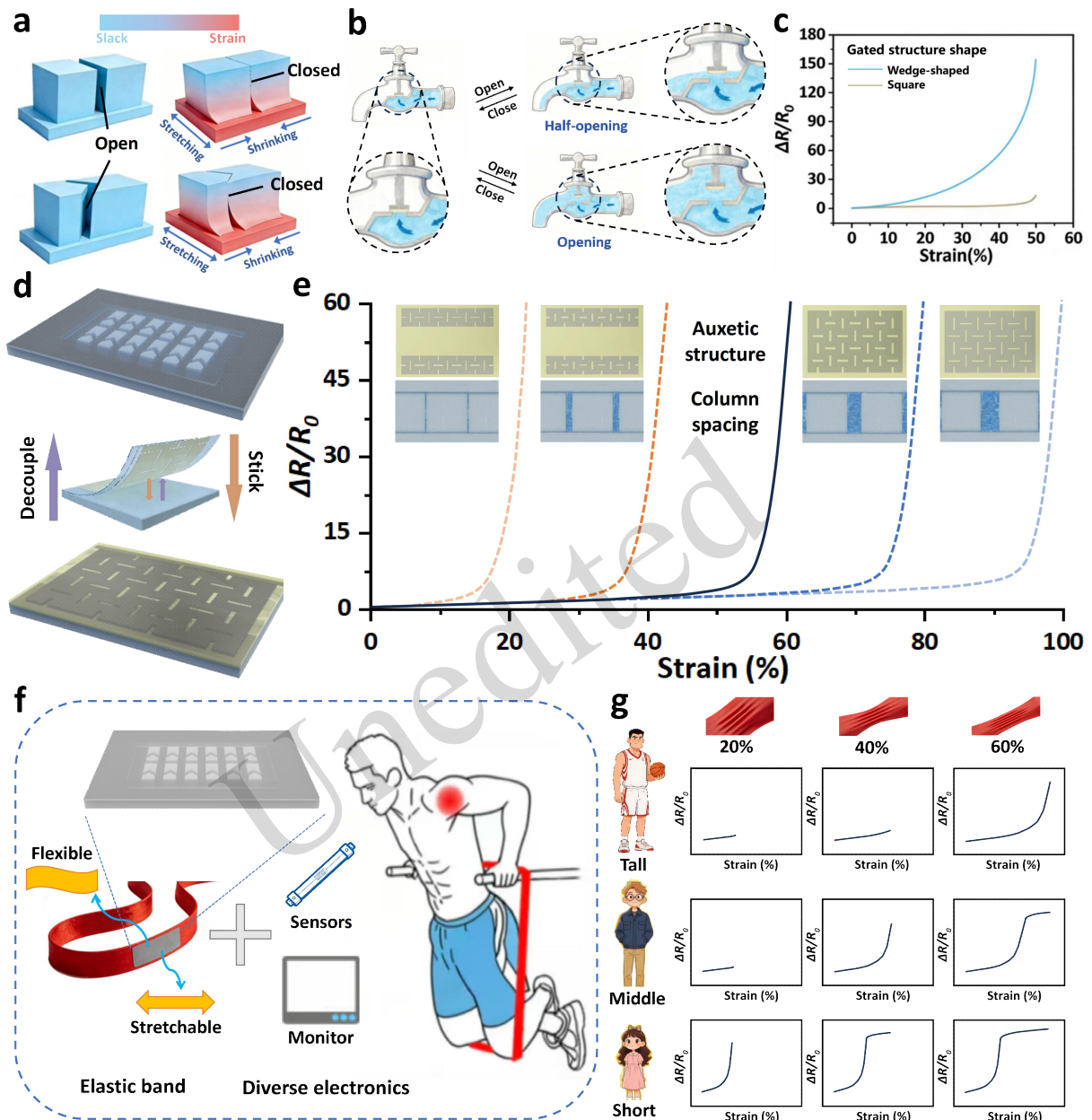


Fig. 1 The design, mechanism, and personalized application of the tunable gated flexible strain sensor. **(a)** Comparison of the tensile closure behavior between wedge-shaped and conventional square micropillars. **(b)** Schematic illustration of the sensing mechanism for the gated architecture. **(c)** Comparing the electrical responses of two distinct gated structures. **(d)** Integration of the detachable negative Poisson's ratio (NPR) metamaterial onto the gated flexible strain sensor. **(e)** Performance modulation of the sensor enabled by various metamaterial configurations. **(f)** An intelligent integrated system comprising a resistance band, the sensor, and a monitoring device for sports applications. **(g)** Personalized adaptation for motion detection of users of different statures.

An intuitive analogy for comprehending the response behavior of the gated sensor is the dynamic regulation of a water faucet valve (Fig. 1b). Like a flow valve, the opening and closure of the sensor's conductive pathway are dictated by mechanical

stretching and releasing. Thus, the gate closure threshold can be reversibly modulated in real time via the attachment or detachment of metamaterial structures (Fig. 1d). Fig. 1e shows a comparison of the sensing performance of the device integrated with

different metamaterial layers. Taking the resistance response curve of the original sensor (black line) as a baseline, a rightward shift in the threshold of the abrupt resistance surge is induced by adding a single perforated plate. In contrast, when the single perforated plate is replaced with double-sided perforated plates, the threshold shifts to the left. Moreover, the magnitude of this threshold shift is highly tunable with the plate dimensions. The sensor's practical potential is validated by constructing a smart resistance band system (Fig. 1f) for human-machine interfaces and health monitoring. Through real-time tracking of the deformation of the resistance band, motion status is monitored and early warnings for injury risks can be issued. Crucially, its warning threshold is tunable on-demand through attachment of different metamaterial layers. This unique feature makes the system easily adaptable to users of varying heights, enabling personalized smart sports protection (Fig. 1g).

3.2 Sensing performance of the wedge-shaped micropillar gated strain sensor

Compared to liquid metals with high surface tension and high viscosity, ionic liquids are a more fluid and sensitive conductive filler for gated strain sensors, responding more sensitively to the closing behavior of the gated structure. To prevent leakage of the ionic liquid, a double-layer structure is employed to ensure robust and stable sensor encapsulation (Fig. 2a). This architecture includes a microchannel layer consisting of a micropillar array and a flat encapsulation layer, which are bonded together to form a sealed microchannel that houses the ionic liquid. After applying tensile strains, no leakage of the ionic liquid is observed (Fig. S1, Supporting Information). Through comparative testing, a 60% concentration of [Emim]BF₄ is identified as the optimal ionic liquid; this is attributed to its superior electrical conductivity, low volatility at room temperature, low viscosity (Figs. S2 and S3, Supporting Information), and favorable resistance response (Fig. S4, Supporting Information). To ensure optimal fluidity of the ionic liquid within the microchannel, the plasma treatment duration is

optimized to minimize the contact angle (Fig. S5, Supporting Information).

The effect of the ionic liquid volume within the microchannel on the electrical response is next investigated under varying strains. As shown in Fig. S6 (Supporting Information), injecting only 1–3 μL of the ionic liquid into the microchannel is sufficient to achieve an excellent resistance response. Unlike square cross-sectional designs, a wedge-shaped micropillar is proposed to optimize the sensing performance through geometric modification (Fig. 2b). To validate the feasibility of this design, Abaqus FEA software is used to simulate the mechanical behavior of both the wedge-shaped and conventional square micropillars under stretching. The simulation parameters and meshing details are provided in Note S1 and Fig. S7 (Supporting Information). As the tensile strain further increases beyond the initial contact point of the micropillars, the contact area between them continuously expands, leading to a drastic reduction in the effective cross-sectional area of the conductive liquid pathway. According to the law of resistance, $R = \rho L/S$, this sharp decrease in cross-sectional area leads to an abrupt surge in resistance, yielding superior sensitivity. Ecoflex 00-30, a silicone material with exceptional tensile properties, is used for the substrate and encapsulation layers. Owing to its intrinsic elongation at breakage far exceeding 100% (reaching up to 400%, as shown in Fig. S8, Supporting Information), this material is utilized to ensure that, even after extreme stretching, the sensor can be fully restored to its original microstructure. Consequently, validation of the wedge-shaped micropillar design for further sensitivity enhancement requires comparing the evolution of the interstitial gap area between micropillars during stretching. A tensile strain of 100% is accordingly applied to both structural models. At each analysis step, the cross-section at the micropillar midpoint is extracted to calculate the gap area (Figs. 2c and 2d). The results show that the wedge-shaped micropillars exhibit a more pronounced reduction in cross-sectional area than their square counterparts under equivalent strain.

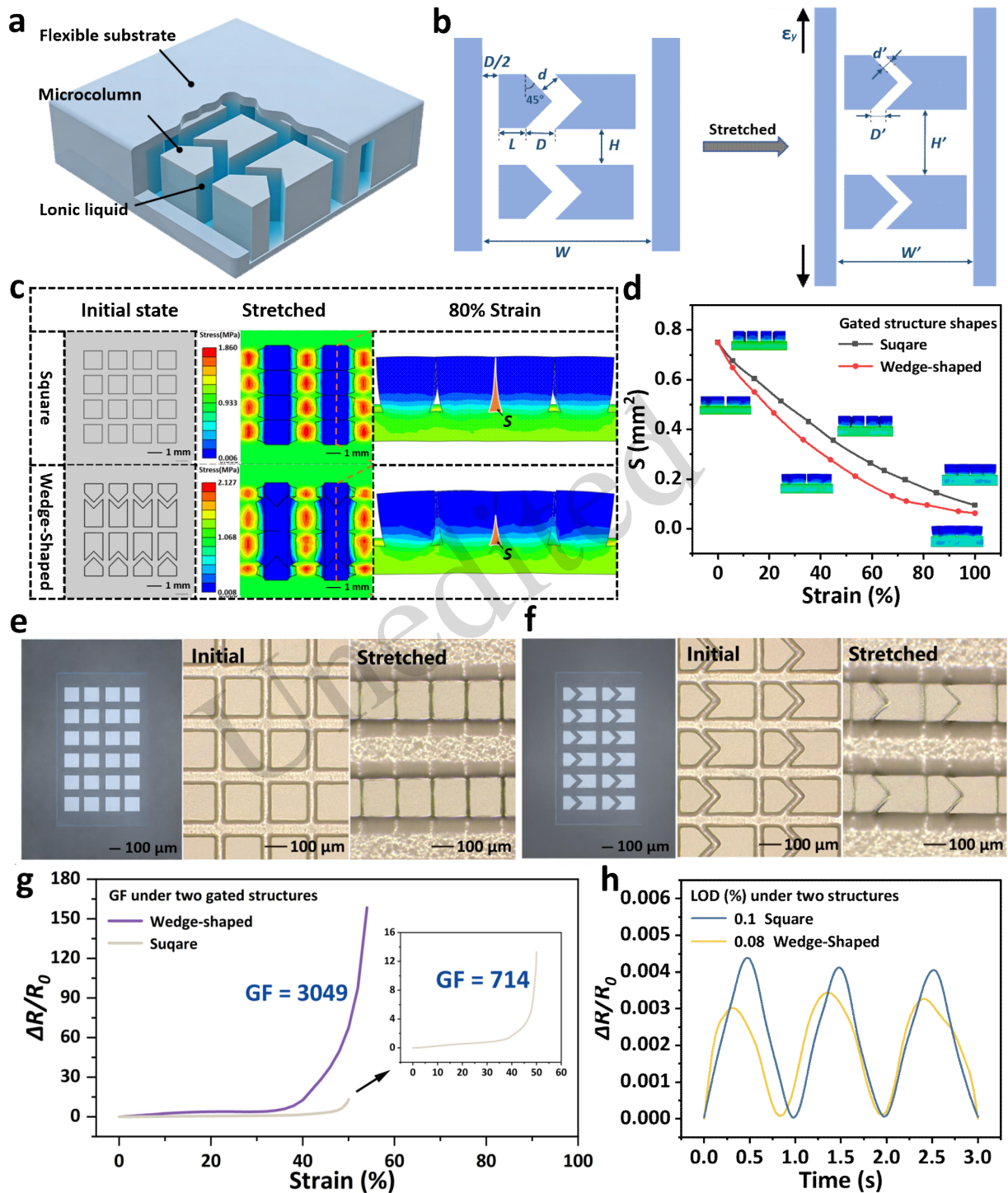


Fig. 2 Structural design, FEA, and experimental characterization of the wedge-shaped gated strain sensor. (a) Schematic diagram of the gated strain sensor featuring a wedge-shaped micropillar architecture. (b) Geometric configurations and dimensional parameters of the wedge-shaped micropillar and microchannel. (c) Stress distribution contours of the wedge-shaped and square micropillar structures under tensile strain. (d) Evolution of the interstitial gap area during the stretching process for both of the micropillar configurations. (e) Confocal microphotographs of the square micropillar structure before and after stretching. (f) Confocal microphotographs of the wedge-shaped micropillar structure before and after stretching. (g) Sensitivity comparison (GF) between the wedge-shaped and square-structured gated strain sensors. (h) Comparison of the limit of detection (LOD) showing the minimum detectable strain for both sensor configurations.

To validate the numerical simulation results, flexible substrates featuring wedge-shaped and square microchannels are fabricated, and the morphological changes of these two configurations before and after stretching are characterized via confocal microscopy (Figs. 2e and 2f). Upon application of longitudinal tensile strain, adjacent micropillars in both structures undergo transverse contraction, ultimately establishing conformal contact. Sensing performance evaluations reveal that the relative resistance change of the wedge-shaped sensor is significantly higher than that of its square counterpart across the entire applied strain range. Notably, the wedge-shaped sensor achieves a maximum sensitivity of 3049, compared to only 714 for the square structure, representing a nearly order-of-magnitude enhancement (Fig. 2g). These experimental results are in excellent agreement with the theoretical predictions derived from finite element analysis regarding the evolution of the cross-sectional area, confirming that the wedge-shaped micropillar architecture significantly enhances the sensitivity of the flexible gated strain sensor. In addition to this remarkable improvement in sensitivity, the wedge-shaped structure demonstrates superior performance in terms of its limit of detection. Testing reveals that its minimum detectable strain is reduced to 0.08%, as compared to the 0.1% observed for the square configuration, further validating the effectiveness of the proposed structural design in elevating overall sensor performance (Fig. 2h).

3.3 Design of the negative Poisson's ratio perforated plate metamaterial

Among the various two-dimensional metamaterial configurations exhibiting negative Poisson's ratio (NPR) – including re-entrant, chiral, rotating rigid, and perforated plate structures – the perforated plate type has been widely adopted in

flexible strain sensors. In such structures, the deformation behavior under mechanical loading is largely determined by the geometry and spatial arrangement of the perforations, which can range from simple periodic circular holes to complex aperiodic patterns. In this work, a perforated plate with rectangular holes was selected as the NPR metamaterial structure for investigation. The geometric parameters of its unit cell include rectangular dimensions of a and b , and a side length of L (Fig. 3a). FEA is performed using *Abaqus*, with the simulation parameters detailed in Note S1 and Fig. S9. The tensile simulation results reveal that both the single unit cell (Fig. 3b) and the macroscopic structure composed of its periodic arrays (Fig. 3c) display a pronounced negative Poisson's ratio effect. This result validates the excellent negative Poisson's ratio characteristics of the rectangular perforated plate architecture.

To systematically investigate the influence of dimensional parameters on the unit cell's Poisson's ratio, the effect of the rectangular hole dimension a is first analyzed. Under a fixed longitudinal tensile strain of 25%, with b and L kept constant, the parameter a is incrementally increased from 0.3 to 0.7 mm. Simulations show that as a grows, the Poisson's ratio of the unit cell displays a monotonically increasing trend, signifying a gradual attenuation of its negative Poisson's ratio effect (Fig. 3d). Using the identical control variable method at a fixed longitudinal tensile strain of 25%, the effects of the parameters b and L are subsequently explored. The results demonstrate that the Poisson's ratio monotonically decreases as b increases (Figs. 3e and S10, Supporting Information), indicating an enhancement of the NPR effect. Conversely, the Poisson's ratio monotonically increases with larger values of L (Fig. 3f), which corresponds to a weakened NPR effect.

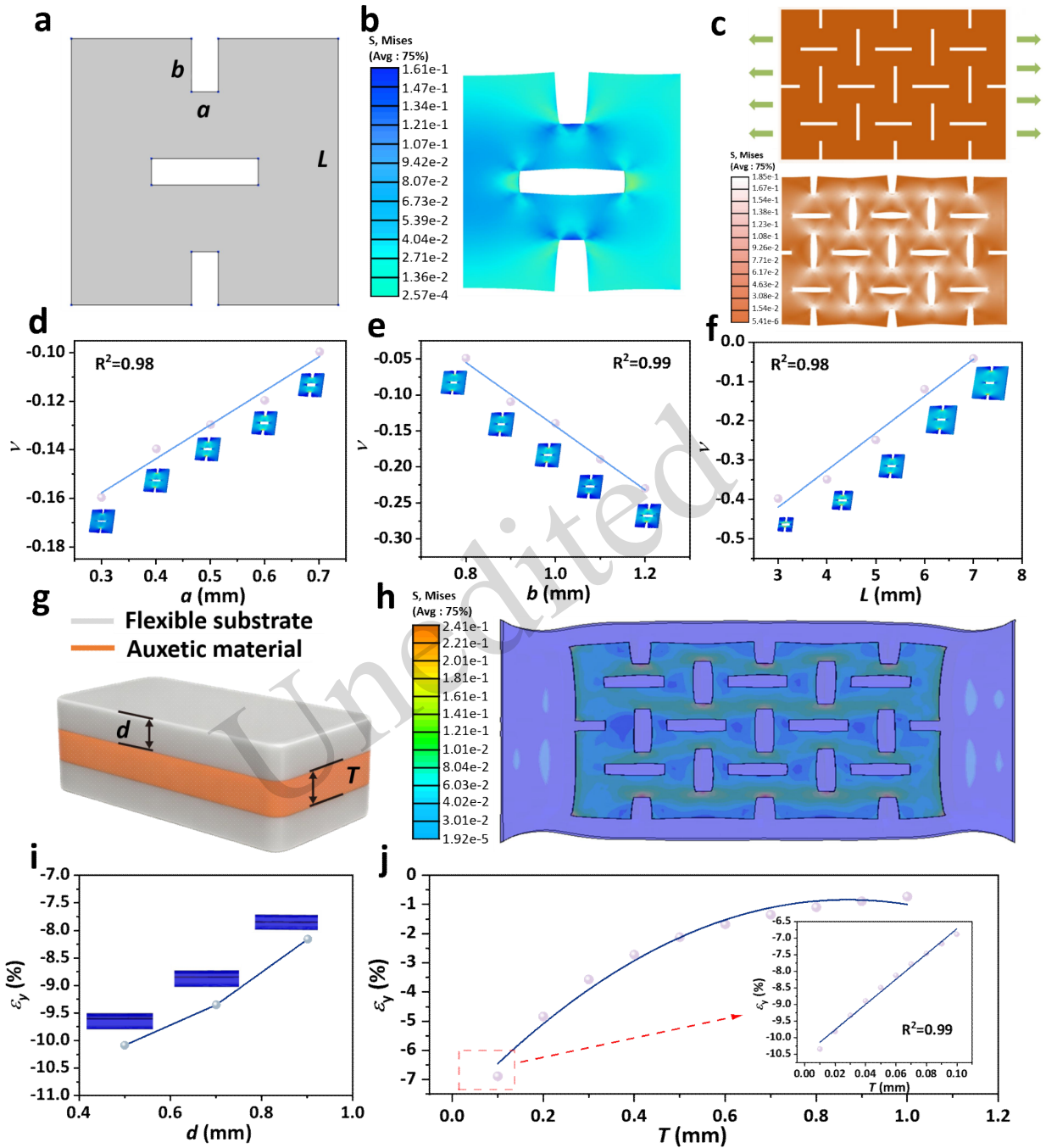


Fig. 3 Design, parametric analysis, and mechanical characterization of the perforated plate metamaterials. **(a)** Geometric parameters of the perforated plate unit cell. **(b)** FEA simulation of an individual unit cell under tensile loading. **(c)** FEA simulation of the perforated plate array (macroscopic structure) under tensile loading. **(d)** Effect of the parameter a on the negative Poisson's ratio (NPR) of the unit cell. **(e)** Effect of the parameter b on the negative Poisson's ratio (NPR) of the unit cell. **(f)** Effect of the parameter L on the negative Poisson's ratio (NPR) of the unit cell. **(g)** Schematic illustration of the flexible substrate embedded with the metamaterial structure. **(h)** Simulation of the NPR effect as manifested by the perforated plate within the flexible matrix. **(i)** Influence of the embedding depth d of the perforated plate on the overall transverse strain. **(j)** Influence of the perforated plate thickness T on the overall transverse strain.

The metamaterial structure is embedded into the flexible substrate (Fig. 3g), where the gray region

represents the flexible polymer matrix and the orange region represents the metamaterial structure with

negative Poisson's ratio characteristics. To select an appropriate material for the perforated plate, the mechanical properties of different materials fabricated via laser cutting or 3D printing are evaluated. Ultimately, Flexible 80A is selected due to its optimal flexibility (Figs. S11, S12, and S13, Supporting Information). During the tensile simulation, the metamaterial structure dominates the overall deformation mode of the assembly through its unique mechanical response. Upon the application of axial tensile strain, the NPR metamaterial structure undergoes transverse expansion. This expansion effect transfers to the surrounding flexible substrate via the interface, causing the entire substrate to exhibit pronounced transverse dilation (Fig. 3h). To investigate the effect of the embedding depth d of the perforated plate within the flexible substrate on the overall tensile behavior, the substrate thickness and the plate thickness are fixed at 2 and 0.3 mm, respectively, and a 25% axial strain is applied to the entire assembly. It is found that increasing the embedding depth d toward the center of the substrate gradually amplifies the overall transverse strain, indicating that the inherent transverse contraction of the flexible substrate is progressively suppressed by the perforated plate; that is, the plate's NPR effect becomes stronger as the embedding depth increases (Fig. 3i). Using the identical control variable method, we further investigate the influence of the perforated plate's thickness on the transverse strain under a fixed substrate thickness of 2 mm, with the plate being embedded in the central layer and subjected to a 25% axial strain. It is revealed that the transverse strain increases monotonically with plate thickness, indicating that the NPR response of the plate is strengthened as its thickness increases, thereby leading to a more pronounced influence on substrate deformation (Fig. 3j).

3.4 Sensing performance tuning based on perforated plate structures

By reversibly attaching and detaching the perforated plate layer on the surface of the gated flexible strain sensor using a flexible 3M tape and an adhesive remover (Fig. 4a), a completely integrated, performance-tunable sensor is constructed. Based on our preceding analysis, tuning the structural parameters, embedding depth, or thickness of the perforated plate effectively alters the Poisson's ratio of the flexible substrate, enabling on-demand modulation of the gated sensor's performance. Taking the variation of the unit cell parameter b as an example, perforated plate layers with varying b dimensions are attached to the sensor surface to evaluate the influence of two different layout configurations on the sensing response. When a single perforated plate is arranged at the bottom of the microchannel, the sensing curve exhibits a rightward shift compared to the original, unattached state (black curve) (Fig. 4c); conversely, adopting a symmetric arrangement on both sides of the microchannel induces a leftward shift in the sensing curve (Fig. 4d). These results demonstrate that full-range tunability of the sensing performance can be realized simply by altering the layout configuration and dimensional parameters of the perforated plates. Furthermore, distinct layout configurations exert differential impacts on the limit of detection (LOD) of the sensor. For instance, attaching a single perforated plate optimizes the LOD, empowering the sensor to detect more subtle strain signals. In contrast, the double-sided symmetric arrangement yields the opposite effect, resulting in compromised LOD performance (Fig. 4e). Regarding the adhesive interface's durability, repeated peel tests indicate that its bonding performance degrades after ten disassembly-assembly cycles (Fig. S14, Supporting Information). However, this issue is easily mitigated, as replacing the 3M tape at the interface fully restores the initial mechanical coupling strength, and the low cost of this keeps replacement expenses minimal.

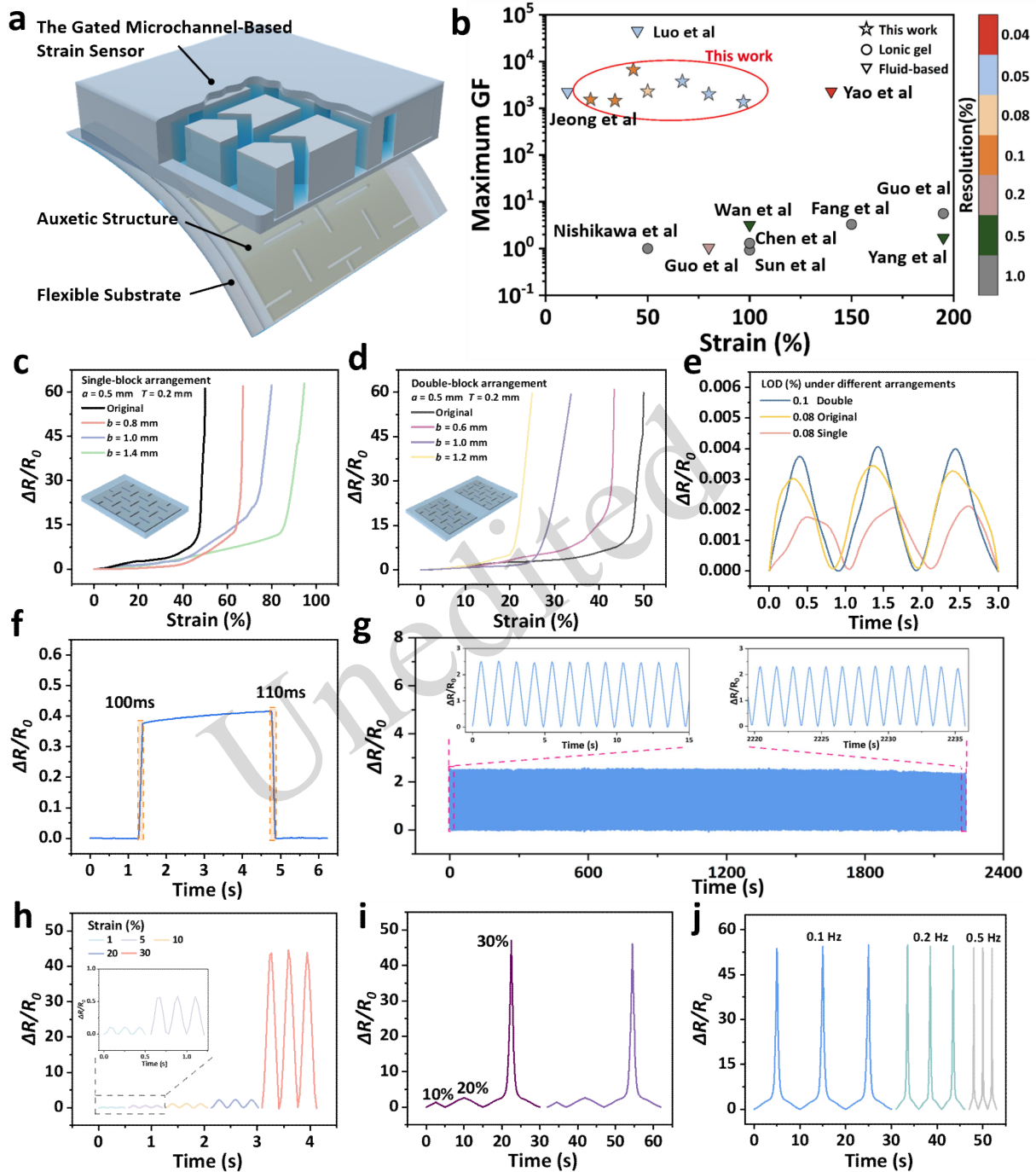


Fig. 4 Performance modulation and dynamic characterization of the metamaterial-integrated gated strain sensor. **(a)** Schematic illustration of the gated flexible strain sensor integrated with the detachable NPR metamaterial. **(b)** Performance comparison between the proposed sensor and previously reported flexible strain sensors. **(c)** Modulation of sensing performance via a single-block metamaterial arrangement. **(d)** Modulation of sensing performance via a double-sided symmetric metamaterial arrangement. **(e)** LOD of various metamaterial arrangements compared to the pristine sensor. **(f)** Response and recovery times of the strain sensor featuring the double-sided symmetric metamaterial configuration. **(g)** Cyclic stability test of the sensor with a double-sided symmetric metamaterial arrangement over 2,000 cycles. **(h)** Strain adaptability of the sensor under various strain levels. **(i)** Cyclic step-strain loading test demonstrating the reliability of the device. **(j)** Frequency-dependent response of the sensor at a constant strain of 30% under varying frequencies (0.1 Hz, 0.2 Hz, and 0.5 Hz).

Next, to evaluate the overall performance of the sensor, dynamic response tests are conducted on the

version of the device integrated with symmetric double-sided metamaterial layers. Under 10% strain, the sensor exhibits response and recovery times of 100 ms and 110 ms, respectively (Fig. 4f). Moreover, regardless of the layout of the integrated metamaterial layers, the signal delay only varies minimally. The overall response time remains excellent at approximately 100 ms, as shown in Fig. S15 (Supporting Information). Benefiting from the sensing mechanism of the gated architecture – which relies on fluidic extrusion and backflow – the device exhibits exceptional stability. Following 2000 continuous loading-unloading cycles at a frequency of 0.8 Hz and 10% strain, the output signal displays negligible variation, demonstrating robust cyclic stability and fatigue resistance (Fig. 4g). Furthermore, the sensor displays excellent long-term stability, even after 30 days (Fig. S16, Supporting Information). In addition, the sensor possesses remarkable strain adaptability, maintaining a stable and consistent response across both small and large strains (Fig. 4h). Under cyclic step-strain loading (Fig. 4i), the output signal remains quite stable, further verifying the reliability of the device. In order to address the variable frequency demands of practical applications, the response characteristics are evaluated under a strain of 30% at varying frequencies (0.1 Hz, 0.2 Hz, and 0.5 Hz), as depicted in Fig. 4j. The sensor delivers stable and reproducible output signals across all tested frequencies, validating its frequency adaptability.

The proposed sensor also exhibits exceptional sensitivity, boasting a maximum gauge factor (GF) that is several orders of magnitude higher than those of typical ionogel-based and liquid-based strain sensors. While certain reported gated sensors achieve comparable or even higher GFs, their micropillar architectures remain static after fabrication, precluding any real-time modulation of their sensing response curves. This inherent imperfection not only makes it exceedingly difficult to ensure device-to-device performance consistency in practice, but also substantially inflates fabrication costs; however, the dynamic tuning strategy effectively overcomes these bottlenecks. The tuning range is exceptionally broad, covering most practical operating conditions. Alongside its high GF and wide

detection range, the device boasts an outstanding limit of detection of 0.05% (Fig. 4b and Table S1, Supporting Information) (Luo et al., 2023; Yao et al., 2024; Guo et al., 2023; Yang et al., 2023; Wan et al., 2019; Jeong et al., 2024; Sun et al., 2020; Nishikawa et al., 2023; Chen et al., 2022; Fang et al., 2025; Guo et al., 2023).

3.5 Motion monitoring and injury prevention applications of the resistance band-integrated system

To fully capitalize on its wide tunability range and superior sensitivity, the proposed sensor is employed for human motion monitoring and sports injury prevention applications. Specifically, the fabricated sensor is integrated onto the surface of a resistance band using a silicone rubber adhesive (Fig. 5a). As the resistance band stretches during human movement, the closely-attached sensor undergoes synchronous deformation, inducing a corresponding variation in its electrical resistance. Accordingly, by monitoring these resistance signals in real time, the stretching state of the band can be accurately captured (Fig. 5b); this enables dynamic tracking of human kinetic behaviors. Generally, for homogeneous and highly elastic resistance bands under tension, the macroscopic strain distribution across their effective length is relatively uniform. Therefore, attaching the sensor to most areas within the middle section yields consistent signals. Given that the ends near the handles are prone to strain gradients caused by localized compression or uneven loading, the sensor is attached to the middle section of the resistance band to guarantee optimal monitoring performance. Overall, the device exhibits excellent environmental robustness under practical exercising conditions. The dense, double-layer Ecoflex encapsulation provides outstanding waterproofing and moisture-proofing performance (Fig. S17, Supporting Information), effectively shielding the ionic liquid from ambient humidity and sweat. Within the typical temperature range of human motion, any minor baseline drift induced by temperature variations is completely masked by the abrupt orders-of-magnitude surge in resistance arising from the gating mechanism, despite slight fluctuations in the ionic liquid's conductivity. This robust property ensures the sensor's reliability in real wearable scenarios.

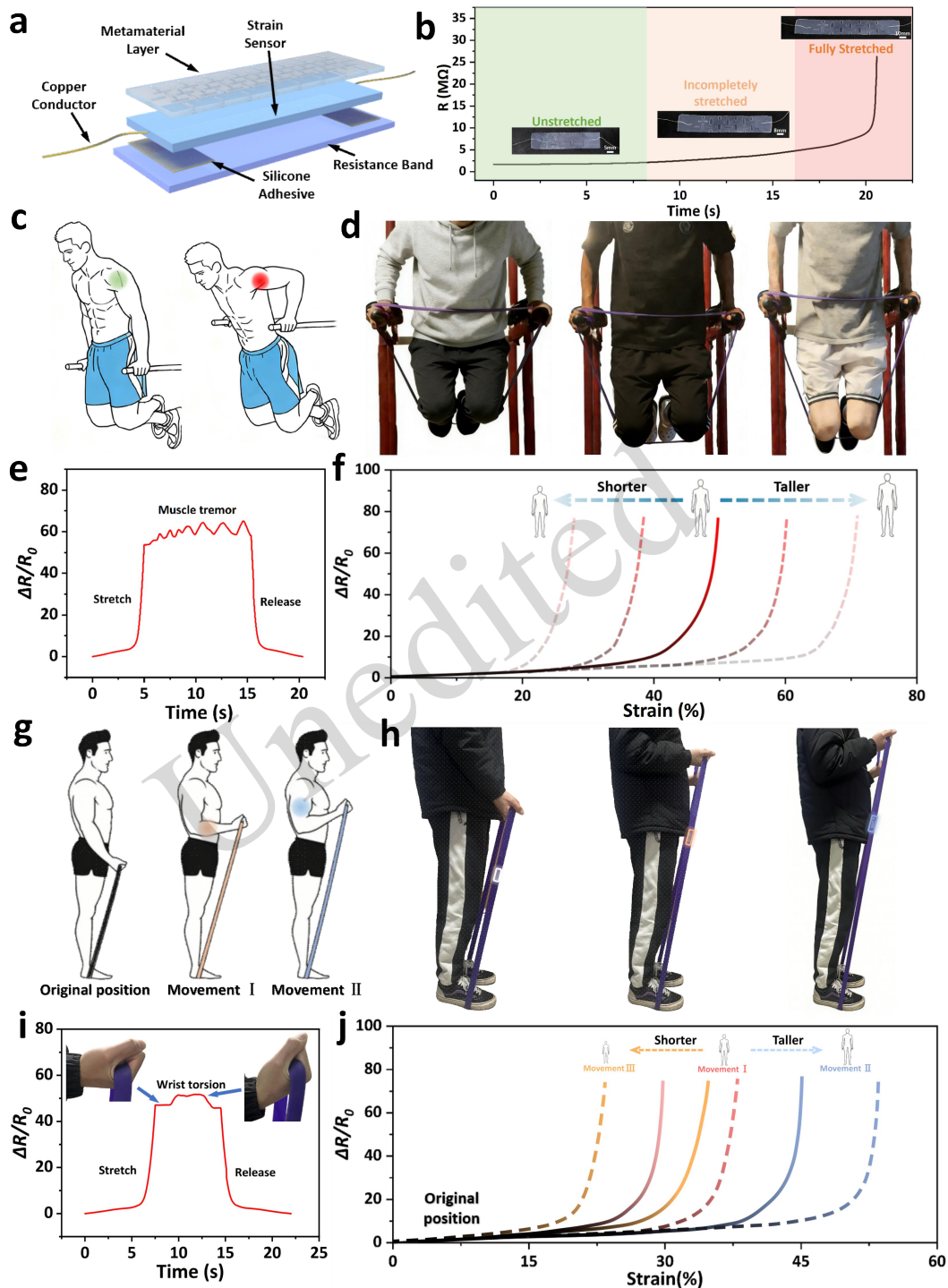


Fig. 5 Practical applications of the smart resistance band-sensor system in personalized motion monitoring and sports safety. (a) Schematic illustration of the integrated smart resistance band-sensor system. (b) Signal response of the smart system to tensile deformation of the resistance band. (c) Application of the smart system for risk assessment during parallel bar dips. (d) Comparison of band elongation for individuals of varying statures performing the exercise. (e) Sensing fatigue-induced tremors during parallel bar dips. (f) Tuning of the sensing performance for parallel bar dip monitoring to accommodate users of different heights. (g) Exercise modalities targeting distinct muscle groups during resistance band-assisted curls. (h) Real-time monitoring of the stretching status of the smart system during the curling exercise. (i) Detection of wrist torsion maneuvers by the smart resistance band system. (j) Personalized performance modulation of the system, adapting to different motion patterns and user statures during curls.

With the goal of demonstrating the sensor's potential for personalized motion monitoring, the parallel bar dip – a representative fitness exercise – is selected for testing (Fig. 5c, Video S1). During the descent phase, this exercise imposes substantial loads on the shoulder joints of the individual, posing a risk of injury due to excessive descent. Therefore, individuals with insufficient strength often rely on a resistance band for assistance during this exercise. However, when users of varying heights use an identical resistance band, the band's elongation differs significantly depending on their stature (Fig. 5d). This inherent variability implies that a sensor with fixed parameters is inadequate for meeting the diverse monitoring requirements of different individuals. To accommodate these needs, the sensor's response profile must be individually tuned (Fig. 5f) to provide accurate early warnings against excessive descent; these can be indicated by an abrupt, step-like surge in the resistance signal. Specifically, for taller users, the detachable NPR metamaterial can be configured to shift the sensing curve rightward, triggering the warning threshold at a higher strain. Conversely, shifting the curve leftward enables responses at reduced strains to accommodate people with shorter statures. This on-demand tuning strategy ensures optimal monitoring and protection across diverse body types. Importantly, the sensor not only captures the large strain signals induced by the gross descent motion, but also precisely resolves subtle deformations originating from involuntary body tremors at the lowest point of the dip (Fig. 5e). This highlights the sensor's ability to detect minute strain fluctuations even under large background deformations, demonstrating exceptional synergy between the broad sensing range and ultrahigh sensitivity.

Beyond early warnings for sports injuries, the sensor may also be employed to evaluate standardization of exercise postures. Taking a resistance band curl exercise as an example (Fig. 5g), variations in the range of motion (ROM) correspond to differences in the targeted muscle groups. Specifically, curling the band until the forearm is parallel to the ground primarily activates the forearm musculature; in contrast, continuing the curl until the forearm forms a 30° angle with the upper arm predominantly targets the biceps brachii. As the

degree of curling varies, the elongation of the resistance band changes accordingly, prompting a corresponding strain response from the sensor (Fig. 5h). Therefore, to accommodate the specific requirements of distinct ROMs and users of varying statures, the sensor's performance can be dynamically tuned to achieve personalization. As presented in Fig. 5j, the red curve denotes the response for ROM I, the blue curve represents ROM II, and the orange curve represents ROM III. The transition from solid to dashed lines illustrates the direction of curve modulation required for adaptation to taller individuals. Similarly, the sensor is capable of detecting subtle wrist torsion following the stretching of the resistance band (Fig. 5i), enabling identification of the distinct phases of the exercise through real-time tuning and monitoring of the response signals (Gul, et al., 2025). This capability empowers the system to meet personalized demands of diverse user groups, demonstrating theoretical significance and broad practical value in the field of intelligent sports monitoring. Meanwhile, benefiting from the core "detachable metamaterial" design, users can easily peel off the 3M tape along with the metamaterial layer when thorough cleaning of the resistance band is required. The waterproof sensor surface and the metamaterial can be directly wiped with a damp cloth and easily reattached once dried.

5 Conclusions

In summary, we have developed a full-range tunable gated flexible strain sensor based on synergistic design of detachable negative Poisson's ratio metamaterials. This strategy resolves the critical bottleneck of traditional gated sensors with regards to their fixed performance and lack of real-time tunability. A robust tuning mechanism for the sensor's response behavior was established by systematically investigating the influence of the perforated plate's geometric parameters on the Poisson's ratio. Furthermore, the wedge-shaped structure is shown to amplify the strain-induced variations in the cross-sectional area, endowing the sensor with both high sensitivity (a gauge factor of 3049) and an ultralow limit of detection (0.05%). Additionally, the gated strain sensor exhibits a fast response time (100

ms), exceptional stability (negligible variation over 2000 cycles), and robust frequency adaptability. The proposed gated strain sensor, with its full-range tunability and high sensitivity, effectively meets requirements of human motion monitoring, indicating its feasibility for sports and health wearable devices.

Acknowledgments

This research was supported by the National Natural Science Foundation of China (U25A20294, 12372168, and 12572184), the National Key Research and Development Program of China (2024YFB3816500), the Natural Science Foundation of Zhejiang Province of China (LQZSZ25E030001, LRG25A020001 and LD26E050001).

Author contributions

Ziao Shen and Minjian Wang designed the research, processed the corresponding data, and wrote the first draft of the manuscript. Xiujun Fu, Guangqiang Zhang and Xiangtao Pan contributed to data collection, analysis, and helped to organize the manuscript. Ye Qiu, Yi Song and Aiping Liu revised and edited the manuscript for technical accuracy. Ye Tian and Huaping Wu supervised the entire research process, revised and edited the final version, and contributed to funding acquisition and project administration.

Conflict of interest

Ziao Shen, Minjian Wang, Xiujun Fu, Guangqiang Zhang, Xiangtao Pan, Ye Qiu, Yi Song, Aiping Liu, Ye Tian and Huaping Wu declare that they have no conflict of interest.

Declaration on the use of generative AI tools

The authors declare that no generative AI tools were used during the preparation of the manuscript.

Data availability

The data that support the findings of this study are available from the corresponding author upon reasonable request.

References

- Dai H, Zhang C, Pan C, et al., 2024. Split-type magnetic soft tactile sensor with 3D force decoupling. *Advanced Materials*, 36(11):2310145. <https://doi.org/10.1002/adma.202310145>
- Yang Q, Li B, Wang M, et al., 2025. Machine learning-enhanced modular ionic skin for broad-spectrum multimodal discriminability in bidirectional human-robot interaction. *Advanced Materials*, 37(42):e08795. <https://doi.org/10.1002/adma.202508795>
- Luo H, Cai Z, Yang G, et al., 2026. Laser-programmed stiffness and interfaces for textile hybrid electronics. *Nature Communications*, 17(1):357. <https://doi.org/10.1038/s41467-025-67149-x>
- Lu Y, Jin Z, Sheng Q, et al., 2026. Universal modulus-free transfer of scalable laser-induced graphene for electronic skins. *Nature Communications*, 17(1):1381. <https://doi.org/10.1038/s41467-025-68131-3>
- Ma J, Wen B, Zhang Y, et al., 2025. Ultra-broad-range pressure sensing enabled by synchronous-compression mechanism based on microvilli-microstructures sensor. *Nature Communications*, 35(35):2425774. <https://doi.org/10.1002/adfm.202425774>
- Yang Y, Meng L, Zhang J, et al., 2024. Near-infrared light-driven MXene/liquid crystal elastomer bimorph membranes for closed-loop controlled self-sensing bionic robots. *Advanced Science*, 11(2):2307862. <https://doi.org/10.1002/advs.202307862>
- Kong D, Lu Y, Zhou S, et al., 2025. Super-resolution tactile sensor arrays with sparse units enabled by deep learning. *Science Advances*, 11(7):eadv21242. <https://doi.org/10.1126/sciadv.adv21242>
- Song Y, Wang JW, Li ZK, et al., 2026. Fingertip-scale six-axis tactile interface with high-precision force sensing and position localization for dexterous human-machine interactions. *Microsystems & Nanoengineering*, 12(1):193. <https://doi.org/10.1038/s41378-026-01292-3>
- Liu H, Li QM, Zhang SD, et al., 2018. Electrically conductive polymer composites for smart flexible strain sensors: a critical review. *Journal of Materials Chemistry C*, 6(45):12121-12141. <https://doi.org/10.1039/c8tc04079f>
- Wang S, Cai W, Wu Y, et al., 2026. A bioinspired multimodal nociceptive system enabling graded pressure-damage pain perception for adaptive robotic interaction. *Chemical Engineering Journal*, 535:175389. <https://doi.org/10.1016/j.cej.2026.175389>
- Qiu Y, Wang F, Zhang Z, et al., 2024. Quantitative softness and texture bimodal haptic sensors for robotic clinical feature identification and intelligent picking. *Science Advances*, 10(30):eadp0348. <https://doi.org/10.1126/sciadv.adp0348>
- Zhang J, Liu S, Wang X, et al., 2024. 4D printable liquid crystal elastomers with restricted nanointerfacial slippage for long-term-cyclic-stability photothermal actuation. *Materials Horizons*, 11(10):2483-2493. <https://doi.org/10.1039/D3MH02230G>
- Luo X, Zhang X, Ji S, et al., 2025. Fully self-healing dual-mode tactile sensing strategy for object's dimension and surface morphology recognition. *Nano Energy*, 136:110757. <https://doi.org/10.1016/j.nanoen.2025.110757>
- Shi C, Zou Z, Lei Z, et al., 2020. Heterogeneous integration of rigid, soft, and liquid materials for self-healable, recyclable, and reconfigurable wearable electronics. *Science Advances*, 6(45):eabd0202. <https://doi.org/10.1126/sciadv.abd0202>
- Lou Z, Wang LL, Jiang K, et al., 2019. Programmable three-dimensional advanced materials based on nanostructures as building blocks for flexible sensors.

- Nano Today*, 26:176-198. <https://doi.org/10.1016/j.nantod.2019.03.002>
- Wang CY, Xia KL, Wang HM, et al., 2019. Advanced carbon for flexible and wearable electronics. *Advanced Materials*, 31(9):1801072. <https://doi.org/10.1002/adma.201801072>
- Shi C, Jiang J, Li C, et al., 2024. Precision-induced localized molten liquid metal stamps for damage-free transfer printing of ultrathin membranes and 3D objects. *Nature Communications*, 15(1):8839. <https://doi.org/10.1038/s41467-024-53184-7>
- Gould J, 2018. Superpowered skin. *Nature*, 563(7732):S84-S85. <https://doi.org/10.1038/d41586-018-07429-3>
- Bayoumy K, Gaber M, Elshafeey A, et al., 2021. Smart wearable devices in cardiovascular care: where we are and how to move forward. *Nature Reviews Cardiology*, 18(8):581-599. <https://doi.org/10.1038/s41569-021-00522-7>
- Ruan D, Chen G, Luo X, et al., 2024. Bionic octopus-like flexible three-dimensional force sensor for meticulous handwriting recognition in human-computer interactions. *Nano Energy*, 123:109357. <https://doi.org/10.1016/j.nanoen.2024.109357>
- Qiu Y, Tian Y, Sun S, et al., 2020. Bioinspired, multifunctional dual-mode pressure sensors as electronic skin for decoding complex loading processes and human motions. *Nano Energy*, 78:105337. <https://doi.org/10.1016/j.nanoen.2020.105337>
- Zhu J, Cheng HY, 2018. Recent development of flexible and stretchable antennas for bio-integrated electronics. *Sensors*, 18(12):4364. <https://doi.org/10.3390/s18124364>
- Yang YY, 2020. A mini-review: emerging all-solid-state energy storage electrode materials for flexible devices. *Nanoscale*, 12(6):3560-3573. <https://doi.org/10.1039/c9nr08722b>
- Lan Y, Li S, Guo H, et al., 2026. Soft biodegradable implants for long-distance and wide-angle sensing. *Nature*, 649(8096):366-374. <https://doi.org/10.1038/s41586-025-09874-3>
- Kang D, Pikhitsa PV, Choi YW, et al., 2014. Ultrasensitive mechanical crack-based sensor inspired by the spider sensory system. *Nature*, 516(7530):222-226. <https://doi.org/10.1038/nature14002>
- Wang Y, Wang L, Yang TT, et al., 2014. Wearable and highly sensitive graphene strain sensors for human motion monitoring. *Nature Communications*, 24(29):4666-4670. <https://doi.org/10.1002/adfm.201400379>
- Yin B, Wen YW, Hong T, et al., 2017. Highly stretchable, ultrasensitive, and wearable strain sensors based on facilely prepared reduced graphene oxide woven fabrics in an ethanol flame. *ACS Applied Materials & Interfaces*, 9(37):32054-32064. <https://doi.org/10.1021/acsami.7b09652>
- Yang H, Ding S, Wang J, et al., 2024. Computational design of ultra-robust strain sensors for soft robot perception and autonomy. *Nature Communications*, 15(1):1636. <https://doi.org/10.1038/s41467-024-45786-y>
- Xing JH, Tao P, Wu ZM, et al., 2019. Nanocellulose-graphene composites: a promising nanomaterial for flexible supercapacitors. *Carbohydrate Polymers*, 207:447-459. <https://doi.org/10.1016/j.carbpol.2018.12.010>
- Zhong X, Jiao W, Liu W, et al., 2024. A novel hollow graphene/polydimethylsiloxane composite for pressure sensors with high sensitivity and superhydrophobicity. *ACS Applied Materials & Interfaces*, 16(20):26674-26684. <https://doi.org/10.1021/acsami.4c01414>
- Qaiser N, Al-Modaf F, Khan SM, et al., 2021. A robust wearable point-of-care CNT-based strain sensor for wirelessly monitoring throat-related illnesses. *Nature Communications*, 31(29):2103375. <https://doi.org/10.1002/adfm.202103375>
- Zhou LY, Fu JZ, Gao Q, et al., 2020. All-printed flexible and stretchable electronics with pressing or freezing activatable liquid-metal-silicone inks. *Nature Communications*, 30(3):1906683. <https://doi.org/10.1002/adfm.201906683>
- Xue P, Chen C, Diao D, 2019. Ultra-sensitive flexible strain sensor based on graphene nanocrystallite carbon film with wrinkle structures. *Carbon*, 147:227-235. <https://doi.org/10.1016/j.carbon.2019.03.001>
- Wang S, Xiao P, Liang Y, et al., 2018. Network cracks-based wearable strain sensors for subtle and large strain detection of human motions. *Journal of Materials Chemistry C*, 6(19):5140-5147. <https://doi.org/10.1039/c8tc00433a>
- Yao WC, Lin XD, Zhang ZS, et al., 2024. Pursuing superhydrophobic flexible strain sensors: from design to applications. *Advanced Materials Technologies*, 9(9):2301983. <https://doi.org/10.1002/admt.202301983>
- Chi K, Zhang ZY, Xi JB, et al., 2014. Freestanding graphene paper supported three-dimensional porous graphene-polyaniline nanocomposite synthesized by inkjet printing and in flexible all-solid-state supercapacitor. *ACS Applied Materials & Interfaces*, 6(18):16312-16319. <https://doi.org/10.1021/am504539k>
- Luo Y, Chen X, Li X, et al., 2023. Heterogeneous strain distribution based programmable gated microchannel for ultrasensitive and stable strain sensing. *Advanced Materials*, 35(2):2207141. <https://doi.org/10.1002/adma.202207141>
- Yao B, Lu X, Wang Y, et al., 2024. Ultrasensitive, highly stable, and stretchable strain sensor using gated liquid metal channel. *Nature Communications*, 34(28):2314298. <https://doi.org/10.1002/adfm.202314298>
- Yao B, Zhu Y, Jin F, et al., 2026. Stretchable strain sensors based on liquid metal channels with simultaneous significant improvements in linearity and sensitivity. *Nature Communications*, 36(12):e17648. <https://doi.org/10.1002/adfm.202517648>

- Wang H, Lyu Y, Bosiakov S, et al., 2023. A review on the mechanical metamaterials and their applications in the field of biomedical engineering. *Frontiers in Materials*, 10:1273961. <https://doi.org/10.3389/fmats.2023.1273961>
- Jiang Y, Liu Z, Matsuhisa N, et al., 2018. Auxetic mechanical metamaterials to enhance sensitivity of stretchable strain sensors. *Advanced Materials*, 30(12):1706589. <https://doi.org/10.1002/adma.201706589>
- Yao G, Mo X, Yin C, et al., 2021. A programmable and skin temperature-activated electromechanical synergistic dressing for effective wound healing. *Science Advances*, 8(4):eab18379. <https://doi.org/10.1126/sciadv.ab18379>
- Mao LN, Pan TS, Ke YZ, et al., 2022. Configurable direction sensitivity of skin-mounted microfluidic strain sensor with auxetic metamaterial. *Lab on a Chip*, 22(8):1630-1639. <https://doi.org/10.1039/d2lc00141a>
- Yan W, Tian X, Zhang D, et al., 2023. 3D printing of stretchable strain sensor based on continuous fiber reinforced auxetic structure. *Chinese Journal of Mechanical Engineering Additive Manufacturing Frontiers*, 2(2):100073. <https://doi.org/10.1016/j.cjmeam.2023.100073>
- Kang M, Choi H, Park K, et al., 2025. Additively manufactured 3D auxetic metamaterials for structurally guided capacitive and resistive tactile sensing. *Nature Communications*, 35(47):e09704. <https://doi.org/10.1002/adfm.202509704>
- Lee JH, Kim YN, Lee J, et al., 2024. Hypersensitive meta-crack strain sensor for real-time biomedical monitoring. *Science Advances*, 10(51):eads9258. <https://doi.org/10.1126/sciadv.ads9258>
- Wang W, Wang X, Li L, et al., 2026. Bioinspired auxetic metastructures enable biomechanically adaptive, machine learning-enhanced self-powered sensing with ultrahigh efficiency. *Nano-Micro Letters*, 18(1):286. <https://doi.org/10.1007/s40820-026-02125-8>
- Shi J, Lu H, Zheng T, et al., 2024. A dynamic phase separation model for glass transition behavior in water-triggered shape memory polymer towards programmable recovery onset. *Journal of Physics D: Applied Physics*, 57(30):305301. <https://doi.org/10.1088/1361-6463/ad4162>
- Shi J, Gorbacheva G, Lu H, et al., 2024. A dynamic trap well model of hydrothermal shape-memory effect in amorphous polymers undergoing tailorable shape recovery behaviour. *Proceedings of the Royal Society A: Mathematical, Physical and Engineering Sciences*, 480(2287):20230615. <https://doi.org/10.1098/rspa.2023.0615>
- Lu H, 2024. When physics meets chemistry at the dynamic glass transition. *Reports on Progress in Physics*, 87(3):032601. <https://doi.org/10.1088/1361-6633/ad2b9c>
- Yao YT, Xu YC, Wang B, et al., 2018. Recent development in electrospun polymer fiber and their composites with shape memory property: a review. *Pigment & Resin Technology*, 47(1):47-54. <https://doi.org/10.1108/PRT-04-2017-0039>
- Yao YT, Luo Y, Xu YC, et al., 2018. Remotely actuated porous composite membrane with shape memory property. *Composite Structures*, 192:507-515. <https://doi.org/10.1016/j.compstruct.2018.03.060>
- Yao YT, Luo Y, Xu YC, et al., 2018. Fabrication and characterization of auxetic shape memory composite foams. *Composites Part B: Engineering*, 152:1-7. <https://doi.org/10.1016/j.compositesb.2018.06.027>
- Zeng J, Jiao W, Wang Y, et al., 2026. Surface engineering on transition metal dichalcogenides: in situ encapsulation of metal-organic frameworks for highly humidity-resistant gas sensing at room temperature. *Advanced Science*, 13(27):e74614. <https://doi.org/10.1002/advs.74614>
- Peng X, Zhou C, Chen K, et al., 2026. Stacking sequence optimization design of CRM wingbox skin structure based on MPSST approach. *Structural and Multidisciplinary Optimization*, 69(1):24. <https://doi.org/10.1007/s00158-025-04228-z>
- Guo H, Lv X, Chen W, et al., 2023. Fabrication of a flexible strain sensor with high-aspect-ratio liquid-metal galinstan. *Advanced Materials Technologies*, 8(1):2200749. <https://doi.org/10.1002/admt.202200749>
- Yang Y, Lv C, Tan C, et al., 2023. Easy-to-prepare flexible multifunctional sensors assembled with anti-swelling hydrogels. *ACS Applied Materials & Interfaces*, 15(39):46417-46427. <https://doi.org/10.1021/acsami.3c11117>
- Wan J, Wang Q, Zang S, et al., 2019. Highly stretchable and sensitive liquid-type strain sensor based on a porous elastic rope/elastomer matrix composite structure. *Composites Science and Technology*, 182:107707. <https://doi.org/10.1016/j.compscitech.2019.107707>
- Jeong J, Mitra A, Lee JB, et al., 2024. Enhancement of sensing range and stability of ultrasensitive crack-based strain sensor using atomized liquid metal. *IEEE Sensors Journal*, 24(6):7284-7291. <https://doi.org/10.1109/JSEN.2023.3295691>
- Sun J, Lu G, Zhou J, et al., 2020. Robust physically linked double-network ionogel as a flexible bimodal sensor. *ACS Applied Materials & Interfaces*, 12(12):14272-14279. <https://doi.org/10.1021/acsami.0c01472>
- Nishikawa T, Yamane H, Matsuhisa N, et al., 2023. Stretchable strain sensor with small but sufficient adhesion to skin. *Sensors*, 23(4):1774. <https://doi.org/10.3390/s23041774>
- Chen J, Wu T, Zhang L, et al., 2022. Flexible ionic-gel strain sensor with double network, high conductivity and high frost-resistance using electrohydrodynamic printing method. *Additive Manufacturing*, 58:103021. <https://doi.org/10.1016/j.addma.2022.103021>

- Fang D, Bian J, Xiang Y, et al., 2025. Self-assembled zwitterionic lignin-induced joint enhancement of mechanics and adhesion in high-performance hydrogels for flexible strain sensors. *Biomacromolecules*, 26(12):8652-8667.
https://doi.org/10.1021/acs.biomac.5c01574
- Guo WY, Mai T, Huang LZ, et al., 2023. Multifunctional MXene conductive zwitterionic hydrogel for flexible wearable sensors and arrays. *ACS Applied Materials & Interfaces*, 15(20):24933-24947.
https://doi.org/10.1021/acsami.3c03919
- Gul O, Song M, Gu CY, et al., 2025. Bioinspired interfacial engineering for highly stretchable electronics. *Nature Communications*, 16(1):1337.
https://doi.org/10.1038/s41467-025-56502-9

Electronic supplementary materials

Video S1, Table S1, Figs. S1–S17

中文概要

题目: 集成可拆卸超材料的性能可调门控应变传感器用于个性化运动识别

作者: 沈子奥^{1,2,3}, 王敏建^{1,2,3}, 傅秀俊^{1,2,3}, 张光强^{1,2,3}, 潘祥涛^{1,2,3}, 袁焯^{1,2,3}, 宋逸^{1,2,3}, 刘爱萍⁴, 田野^{1,2,3}, 吴化平^{1,2,3}

机构: ¹浙江工业大学, 机械工程学院, 中国杭州, 310023; ²浙江工业大学, 全省高精高效复合加工技术与装备重点实验室, 中国杭州, 310023; ³浙江工业大学, 特种装备制造与先进加工技术教育部重点实验室, 中国杭州, 310023; ⁴浙江理工大学, 光电材料与器件中心, 中国杭州, 310018

目的: 开发兼具高灵敏度和宽传感范围的门控应变传感器对于医疗监护、运动监测以及人机交互等任务至关重要。然而, 传统门控传感器在制备后缺乏实时可调性, 且可调范围有限。本文基于可拆卸负泊松比超材料的协同设计, 开发了一种全范围可调的门控柔性应变传感器。

创新点: 1. 集成可拆卸负泊松比超材料与门控应变传感器, 实现传感响应区间的双向实时可逆调控。2. 设计楔形微柱门控结构, 将最高灵敏度提升至 3049, 最小检测应变降至 0.08%。3. 构建“弹性带-传感器-监测”集成系统, 精准监测双杠臂屈伸、弯举等动作并适配不同身高, 为运动损伤预防与健康监测提供新方案。

方法: 1. 基于 Abaqus 有限元仿真, 验证了楔形微柱提升灵敏度的力学机理, 并分析了矩形穿孔板超材料的单胞参数、埋设深度及厚度对泊松比和横向应变的影响。2. 通过实验优化了制备工艺, 筛选出最优离子液体, 确定了等离子处理时长与填充量, 制备了楔形微柱门控式传感器及不同参数的负泊松比超材料贴合层。3. 通过传感性能测试, 对比了楔形与方形微柱的灵敏度及检测极限, 分析了超材料排布方式对响应区间与检测极限的调控效果, 并测定了响应时间、循环稳定性、应变及频率适应性。4. 通过将传感器集成于弹力带构建运动监测系统, 测试了双杠臂屈伸、弯举等动作的信号响应, 验证了更换超材料层可实现不同身高人群的个性化运动监测与损伤预警。

结论: 1. 基于可拆卸负泊松比超材料的协同设计, 开发了一种全量程可调谐的门控柔性应变传感器。2. 通过系统研究穿孔板几何参数对泊松比的影响, 建立了一种用于调控该传感器响应行为的可靠机制。3. 楔形结构可放大应变引起的横截面积变化, 赋予传感器高灵敏度 (应变系数为 3049) 和超低检测限 (0.05%)。4. 该门控应变传感器响应时间快 (100 毫秒)、稳定性极佳 (2000 次循环后变化可忽略不计) 且频率适应性强。

关键词: 应变传感器; 门控结构; 负泊松比; 高灵敏度; 宽传感范围; 小应变检测; 个人健康监测; 可穿戴智能运动传感器